

# Emergent universal statistics in nonequilibrium systems with dynamical scale selection

Vili Heinonen,<sup>1,2</sup> Abel J. Abraham,<sup>3</sup> Jonasz Słomka,<sup>4</sup> Keaton J. Burns,<sup>1</sup> Pedro J. Sáenz,<sup>3</sup> and Jörn Dunkel<sup>1</sup>

<sup>1</sup>*Department of Mathematics, Massachusetts Institute of Technology,  
77 Massachusetts Avenue, Cambridge, MA 02139, USA*

<sup>2</sup>*Department of Mathematics and Statistics, University of Helsinki,  
P.O. Box 68, FI-00014 Helsingin yliopisto, Finland*

<sup>3</sup>*Department of Mathematics, University of North Carolina at Chapel Hill,  
120 E Cameron Avenue, Chapel Hill, NC 27599, USA*

<sup>4</sup>*Institute of Environmental Engineering, Department of Civil, Environmental,  
and Geomatic Engineering, ETH Zurich, 08093 Zurich, Switzerland*

(Dated: May 4, 2022)

Pattern-forming nonequilibrium systems are ubiquitous in nature, from driven quantum matter and biological life forms to atmospheric and interstellar gases. Identifying universal aspects of their far-from-equilibrium dynamics and statistics poses major conceptual and practical challenges due to the absence of energy and momentum conservation laws. Here, we experimentally and theoretically investigate the statistics of prototypical nonequilibrium systems in which inherent length-scale selection confines the dynamics near a mean energy hypersurface. Guided by spectral analysis of the field modes and scaling arguments, we derive a universal nonequilibrium distribution for kinetic field observables. We confirm the predicted energy distributions in experimental observations of Faraday surface waves, and in quantum chaos and active turbulence simulations. Our results indicate that pattern dynamics and transport in driven physical and biological matter can often be described through monochromatic random fields, suggesting a path towards a unified statistical field theory of nonequilibrium systems with length-scale selection.

Nonequilibrium systems balance energy uptake and dissipation to create complex dynamical structures across a wide range of length and time scales<sup>1</sup>, from turbulent flows<sup>2</sup> in driven quantum<sup>3</sup> and classical<sup>4</sup> fluids to the self-organized vortex patterns in active suspensions<sup>5,6</sup>. Recent major advances in the theoretical<sup>7–9</sup> and computational<sup>10</sup> modeling of nonequilibrium pattern-forming phenomena<sup>11,12</sup> have led to a substantially improved understanding of transport processes in physics<sup>4,13</sup> and biology<sup>14,15</sup>. Despite such progress, however, there currently exists no unifying statistical field theory for far-from-equilibrium systems<sup>9,16–19</sup> on par with equilibrium thermodynamics. Perhaps the most fundamental difficulty in identifying universal nonequilibrium statistical principles lies in the fact that systems can be driven out of equilibrium in various ways<sup>1</sup>. Among the most widely studied driving mechanisms are temperature<sup>1,9,20</sup> and pressure<sup>21</sup> gradients, mechanical<sup>22–24</sup> or electromagnetic<sup>25</sup> forcing protocols, and chemical reservoirs<sup>26–28</sup>. This diversity, combined with the absence of conservation laws, makes it challenging to find common statistical descriptions for these systems.

Here, we report progress on this longstanding problem by focusing on pattern-forming systems in which an intrinsic length-scale selection mechanism<sup>1</sup> effectively reduces the number of microscopic degrees of freedom. This large subclass of nonequilibrium systems comprises a broad spectrum of physically and biologically important phenomena, including hydrodynamic and elastic instabilities<sup>22,23,31–39</sup>, liquid–solid phase transitions in quantum superfluids<sup>40–42</sup> and active turbulence<sup>6,43–45</sup>. By combining experiments, theory and large-scale sim-

ulations, we demonstrate that the competition between scale selection and nonlinear mode-mixing can lead to the emergence of universal superstatistics<sup>46</sup> for the relevant energetic field observables. Specifically, our results show that periodically forced Faraday waves<sup>23,32</sup> on the surface

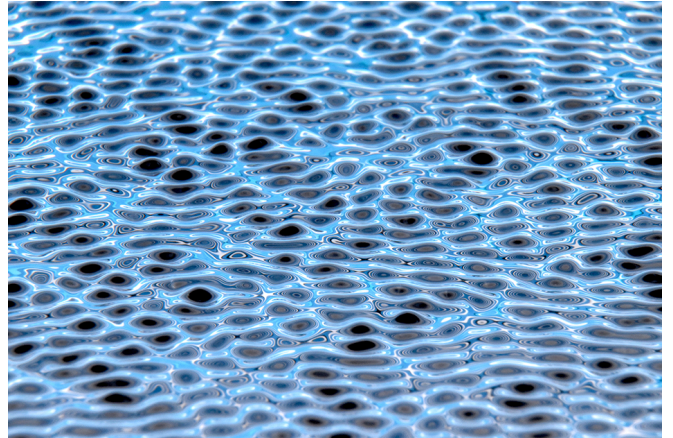


FIG. 1. **Weakly chaotic Faraday surface waves exhibiting scar patterns.** Faraday waves emerging on a vertically oscillating bath of water (Movies 1 and 2, Methods) are representatives of a broader class of non-equilibrium systems with spontaneous scale selection. The photograph shows an oblique view of the fluid surface<sup>29</sup>. The shadows cast by larger wave crests give rise to dark scar-like patterns corresponding to regions of higher surface-gradient energy. In our experiments, the dynamically evolving surface height fields were reconstructed using a free-surface Schlieren technique<sup>30</sup> (Methods). Faraday wavelength:  $\lambda_F \approx 4.6$  mm (Methods).

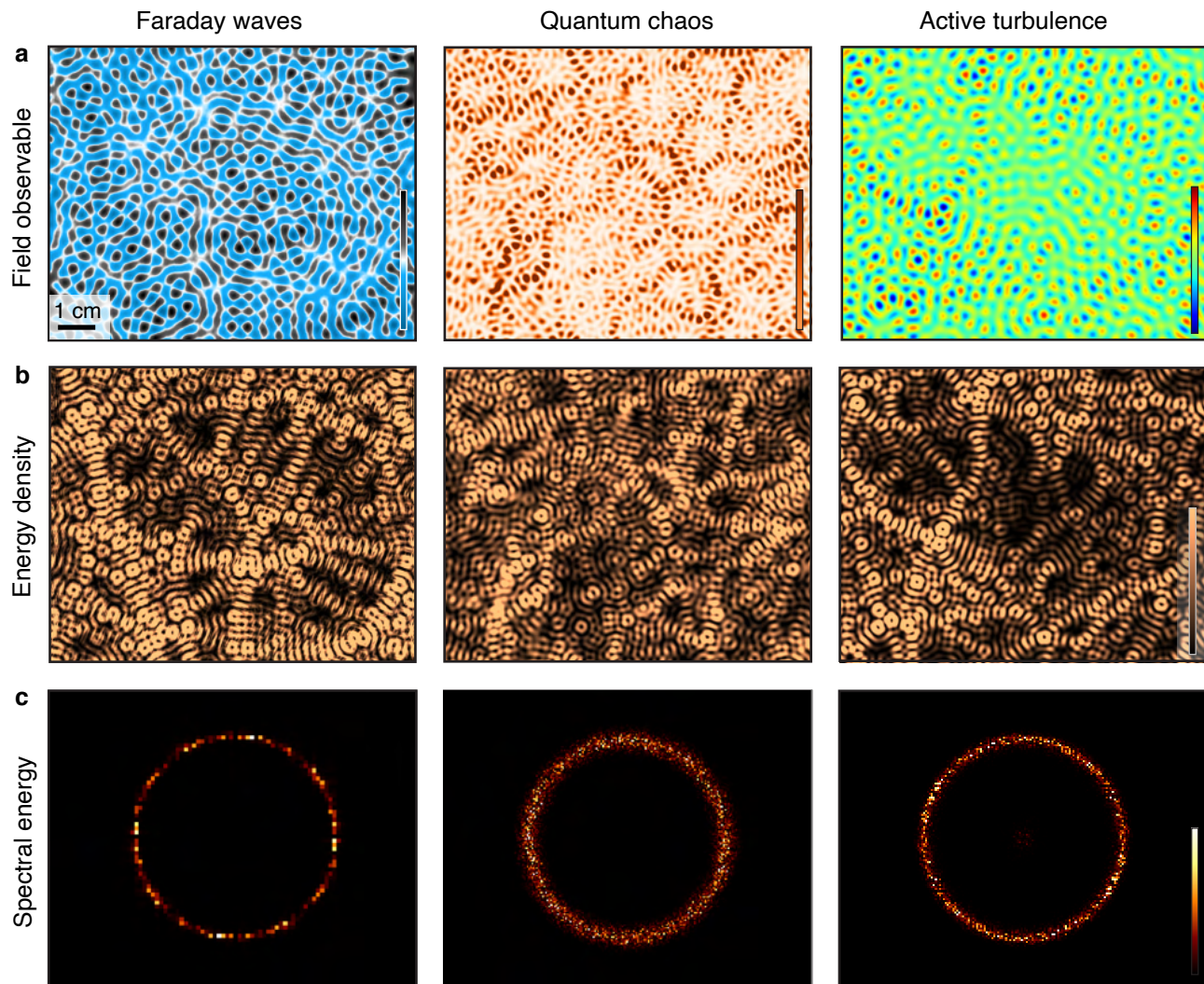


FIG. 2. **Non-equilibrium field dynamics with length scale selection in experiment and simulations.** **a**, Snapshots from our Faraday wave experiments (Fig. 1 and Movie 2), quantum chaos simulations in a smooth isotropic random potential (Eq. 1, Movie 3), and active turbulence simulations (Eq. 2, Movie 4). Colors indicate the normalized height field  $h$ , number density  $|\psi|^2$  and vorticity field, respectively. **b**, Associated energy densities reveal qualitatively similar structures across the different systems: the surface gradient energy of the Faraday waves, and the kinetic energies of the quantum and active fluid systems are characterized by scars extending throughout the system. **c**, Spectral energy density shows that the energy of the system is concentrated within a narrow shell of a fixed wave-number radius. Each panel represents a typical snapshot of the dynamical system at a time much larger than the initial relaxation period. See Methods for details and parameters of experiments, simulations and colorbar limits.

of water (Fig. 1, Movies 1 and 2), chaotic quantum dynamics (Movie 3), and active turbulence (Movie 4) can be jointly described through monochromatic random fields. Building on this insight, we illustrate the practical potential for modeling nonequilibrium transport processes by constructing a generalized Langevin dynamics for passive tracer particles advected by a dense active microbial suspension.

The unified statistical description of the three vastly different nonequilibrium systems (Fig. 2a) investigated here becomes possible because, in each case, self-organized dynamical length-scale selection (Fig. 2b) con-

centrates the mode energies in a narrow circular shell in Fourier space (Fig. 2c). In position space, the distinct scale selection and mode interaction mechanisms governing Faraday waves, quantum chaos and active turbulence manifest themselves as visually similar, dynamically evolving scar-like structures<sup>47</sup> in the local energy densities (Fig. 2b). Our combined experimental, theoretical and numerical analysis suggests that a wide range of nonequilibrium systems displaying such a phenomenology can be described by the same universal energy statistics.

In our experiments, we studied the dynamics of Fara-

day surface waves<sup>23,32,33</sup> on a vertically vibrated water bath (Movie 1). In this parametrically-excited system, the energy injected by the external periodic forcing is balanced by internal viscous dissipation<sup>34</sup>. Owing to the oscillatory nature of the effective gravitational acceleration  $G(t) = g + D \cos(\omega t)$  acting on the fluid, the flat free surface becomes unstable to subharmonic waves when the driving amplitude  $D$  exceeds the critical Faraday threshold  $D_F$ . At threshold, the competition between gravity and surface tension  $\sigma$  results in a preferred Faraday wavelength  $\lambda_F = 2\pi/k_F$  dictated by the standard water-wave dispersion relation  $(\omega/2)^2 = gk_F + \sigma k_F^3/\rho$ , where  $\rho$  denotes the liquid density<sup>34</sup> (Methods). Our statistical analysis below is based on 3D surface measurements (Movie 1) of weakly nonlinear Faraday waves emerging in the super-critical driving regime<sup>32</sup> in which the scarred wave patterns evolve chaotically while maintaining a dominant Faraday wavelength  $\lambda_F \approx 4.6$  mm (Fig. 2a and Movie 2; Methods).

Dynamically evolving scarred patterns<sup>47,48</sup> similar to those observed in Faraday waves arise in 2D quantum chaos<sup>49</sup> described by the Schrödinger hydrodynamic equations (Movie 3)

$$\partial_t \mathbf{v} + \mathbf{v} \cdot \nabla \mathbf{v} = -\frac{1}{m} \nabla(Q + V), \quad (1a)$$

$$\partial_t \rho = -\nabla \cdot (\rho \mathbf{v}), \quad (1b)$$

where the number density  $\rho(t, \mathbf{x}) = |\psi(t, \mathbf{x})|^2$  and the velocity field  $\mathbf{v}(t, \mathbf{x}) = \nabla S(t, \mathbf{x})/m$  are related to the quantum wave function  $\psi = \sqrt{\rho} \exp(iS/\hbar)$ .  $Q = -\hbar^2(\nabla^2 \sqrt{\rho})/(2m\sqrt{\rho})$  is the quantum potential and  $V(\mathbf{x})$  is a smooth random potential that facilitates energy exchange between the momentum modes  $e^{i\mathbf{k} \cdot \mathbf{x}}$ . We simulated Eqs. (1a, 1b) on a large periodic domain of size  $L \times L$  with an initial uniform plane wave with momentum  $\hbar \mathbf{k}_c$ . After a relaxation period  $t_{qc} \sim 0.8 mL^2/\hbar$  (Methods), the quantum state became isotropic due to quasi-elastic wave scattering<sup>49</sup> by the smooth random potential  $V$  (Fig. 2; Movie 3) with a long-range Gaussian correlation function, zero mean, and small variance compared to the initial wavepacket energy (Supplementary Fig. S7). Therefore, the emergent pattern length scale (Fig. 2b) and the radius of the energy shell in Fourier space (Fig. 2c) are determined by  $k_c$ , but not by the external scattering potential  $V$  (Methods) which acts as an energy reservoir for the momentum modes.

Another entirely different nonequilibrium process exhibiting similar energy localization in Fourier space is active turbulence, as seen in dense bacterial suspensions<sup>6,43,44</sup>. This widely studied phenomenon belongs to a broader class of linearly forced fluid flows, which also encompasses nonlinear seismic wave propagation<sup>50</sup> and soft-mode turbulence<sup>51</sup> (Nikolaevskiy chaos). An effective phenomenological description of such pattern-forming flows is given by the linearly forced Navier-Stokes

equations<sup>50-52</sup> (Movie 4)

$$\partial_t \mathbf{v} + \mathbf{v} \cdot \nabla \mathbf{v} = -\nabla p + \nabla \cdot \boldsymbol{\sigma}, \quad (2a)$$

$$\nabla \cdot \mathbf{v} = 0, \quad (2b)$$

where  $p(t, \mathbf{x})$  is the local pressure, and the 2D incompressible velocity field  $\mathbf{v}(t, \mathbf{x}) = (\partial_y \psi, -\partial_x \psi)$  is determined by its stream function  $\psi(t, \mathbf{x})$ . The phenomenological stress tensor  $\boldsymbol{\sigma}(t, \mathbf{x}) = (\Gamma_0 - \Gamma_2 \nabla^2 + \Gamma_4 \nabla^4)[\nabla \mathbf{v} + (\nabla \mathbf{v})^T]$  with  $\Gamma_0, \Gamma_4 > 0$  and  $\Gamma_2 < 0$  accounts for viscous dissipation and microscale energy injection from an active component, such as swimming microbes, into the fluid medium<sup>50-52</sup>. Energy transfer from active to dissipative modes occurs through the advective nonlinearity in Eq. (2a). In qualitative agreement with experimental observations for bacterial suspensions<sup>6,43,52</sup>, Eqs. (2) predict flows with a typical vortex size  $\Lambda = \pi \sqrt{2\Gamma_4/(-\Gamma_2)} = \pi/k_c$  that exhibit scar patterns in the vorticity field  $\omega = \nabla \times \mathbf{v}$  (Fig. 2a right; Movie 4).

Despite their fundamental physical differences and nonequilibrium nature, we found that Faraday waves, 2D quantum chaos and active turbulence are representatives of a joint statistical class whose essential energetic properties can be predicted from basic energy and symmetry considerations. To make this statement precise, we start by noting that all three systems possess a field-deformation energy of the form

$$E(t) \propto \int d\mathbf{x} \frac{1}{2} |\nabla \psi|^2. \quad (3)$$

For Faraday waves,  $\psi$  is the surface height field and  $E$  the surface energy. In quantum chaos,  $E$  is the kinetic energy of the complex-valued wave function  $\psi$ . In active turbulence,  $\psi$  is the real-valued stream function and  $E$  is the kinetic energy of the suspension. In terms of the wave vectors  $\mathbf{k}$  and Fourier-amplitudes  $\hat{\psi}_{\mathbf{k}}(t)$ , the energy (3) can be expressed as

$$E(t) = CA \sum_{\mathbf{k}} \frac{k^2}{2} |\hat{\psi}_{\mathbf{k}}(t)|^2 =: \sum_{\mathbf{k}} \mathcal{E}_{\mathbf{k}}(t), \quad (4)$$

where  $A$  is the size of the system and  $C$  is a system-specific constant (Methods).

We now formulate the three general key criteria that enable statistical predictions for pattern-forming nonequilibrium systems with energies of the form (4): First, the dominant energy amplitudes  $\mathcal{E}_{\mathbf{k}} = C(k^2/2)|\hat{\psi}_{\mathbf{k}}|^2$  fall into a narrow shell around the typical pattern wave number  $k_c$  (Figs. 2c). Second, once the dynamics have settled into a statistically stationary state, the steady-state energy fluctuations are small,  $\Delta E/E_{ave} \ll 1$ . Third, the system is quasi-ergodic, populating each energy mode  $\mathcal{E}_{\mathbf{k}}$  respecting the symmetries of the system (in our case, each of the three systems is isotropic). All three criteria are satisfied by our three example systems (Fig. 2c and SI). Taken together, these criteria force a long-time statistical equilibrium on the

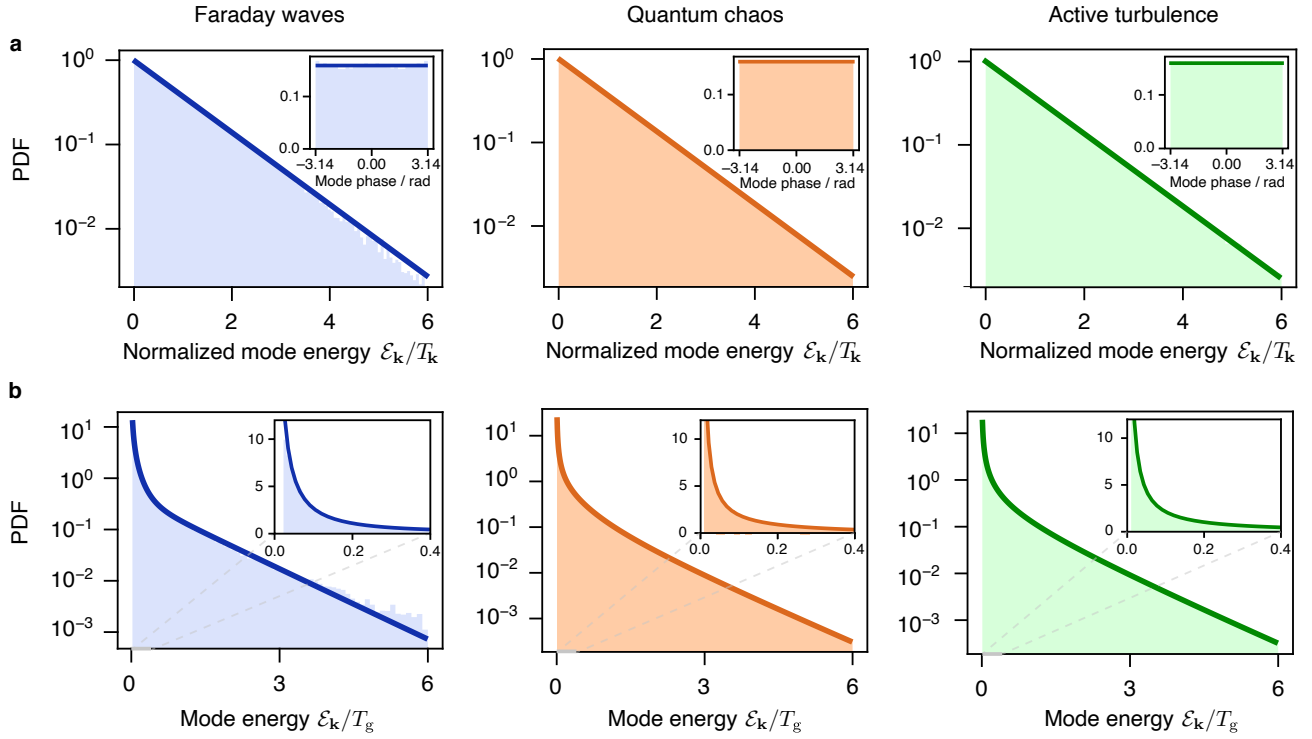


FIG. 3. **Emergent universal statistics in experiment and simulations.** **a**, Energy distribution functions for a representative subset of individual energy modes follow exponential Boltzmann distributions with different mode temperatures. The figures show the statistics for individual modes normalized by the mode temperature  $T_{\mathbf{k}} = \langle \mathcal{E}_{\mathbf{k}} \rangle_t$ . Insets: all systems show uniform statistics for phases of Fourier modes. See Methods for details and parameters of experiments and simulations. **b**, Probability distribution functions (PDFs) of the Fourier mode energies  $\mathcal{E}_{\mathbf{k}}$  measured in the experiment (blue) and simulations (orange, green) follow the predicted superstatistics (solid lines) given by Eq. (5) with system specific global temperatures  $T_g$ . Insets: blow-ups of the energy statistics at low energies shown on a linear scale. See also SI Figs. S4-S8 for additional analysis of the energy distributions.

narrow ring where the individual modes are in equilibrium with an *effective* mode-dependent temperature  $T_{\mathbf{k}}$  following the usual Boltzmann statistics (Fig. 3a). The overall energy statistics arise as superstatistics<sup>46</sup> of the individual Boltzmann statistics. Considering statistically isotropic systems, and combing a Gaussian steepest descent approximation with exponential tail asymptotics, one can derive the overall energy probability density (SI

$$f(\mathcal{E}) = C_f \left( \frac{e^{-\beta_t \mathcal{E}}}{\mathcal{E} \sqrt{\log(\beta_t T_g)}} + T_g \int_{1/T_g}^{\beta_t} d\beta \frac{e^{-\beta \mathcal{E}}}{\sqrt{\log \beta T_g}} \right), \quad (5)$$

where  $C_f$  is a normalization constant and  $\beta_t$  is a tail inverse temperature obtained from fitting to the data (see Methods for the fitting procedure). The Boltzmann constant  $k_B$  is set to unity throughout, defining the units for the temperature. Furthermore, since Eq. (4) does not depend on the phases of  $\psi_{\mathbf{k}}$ , the phases are predicted to follow a uniform distribution.

To test these predictions, we measured the probability density distribution functions (PDFs) of the mode energies  $\mathcal{E}_{\mathbf{k}}$  and the phases  $S_{\mathbf{k}} = \arg \hat{\psi}_{\mathbf{k}}$  in the experiment and simulations. For all three studied systems, we found

close agreement between the theory and data (Fig. 3): The mode energies of Faraday waves, 2D quantum chaos and active turbulence follow the universal superstatistics distributions given by Eq. (5) with a system specific global temperature  $T_g$  (see Methods), and the phases  $S_{\mathbf{k}}$  are uniformly distributed in each case. Generally, Eq. (5) can be expected to provide an accurate description whenever the spectral energy density is focused within a sufficiently narrow ring (Fig. 2c) in Fourier space (Fig. S10 and S11).

While the emergence of universal statistics in pattern-forming nonequilibrium systems with scale-selection is rather remarkable in itself, it also opens a path to an efficient field-statistical description of transport processes that avoids explicit simulations of the underlying field dynamics. To demonstrate this, we focus in the remainder on the advection of passive scalars in active turbulence, a process relevant to nutrient transport and mixing in microbial suspensions<sup>6,43</sup>. Specifically, we show how one can construct an effective Langevin-type description for tracer dynamics by building on the above results. As a reference process, we simulated the dynamics  $\mathbf{X}(t)$  of passive particles advected by the solutions  $\mathbf{v}(t, \mathbf{x})$  of the

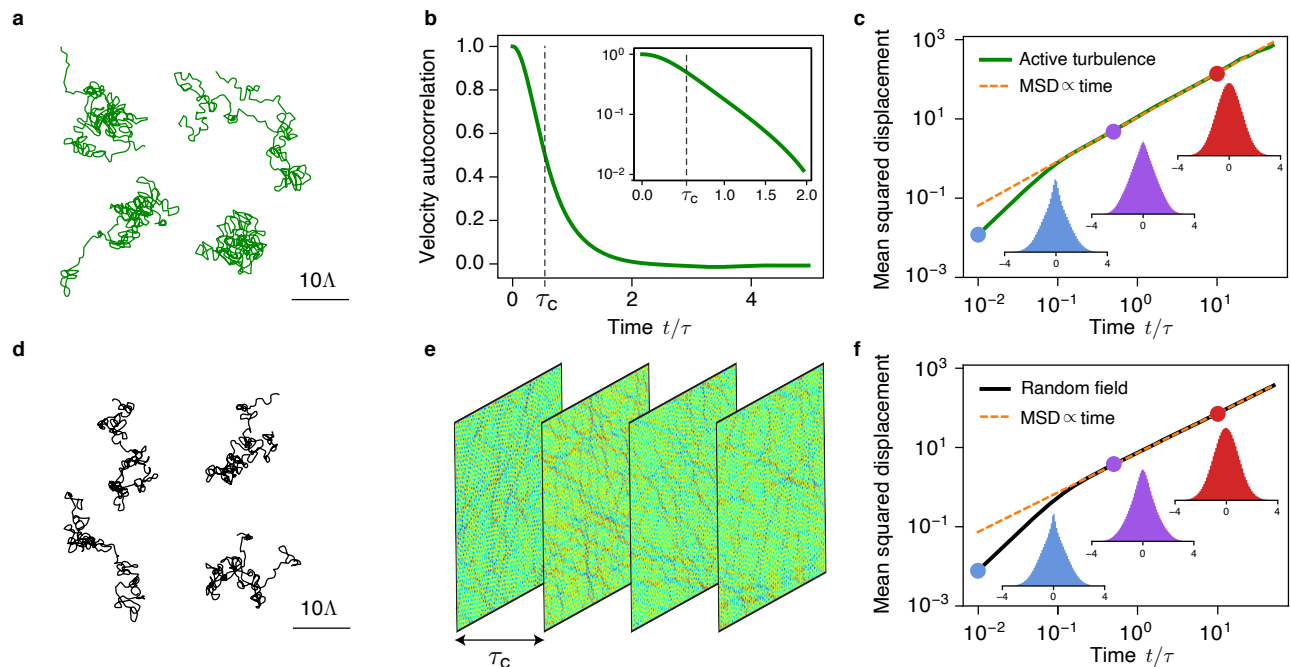


FIG. 4. **Estimating active transport by sampling from monochromatic random fields.** **a**, Example trajectories of passive tracer particles advected by active turbulent flow solutions (Fig. 2a) of the linearly forced Navier-Stokes equations (2). Trajectories are calculated for total time  $50\tau$ , where  $\tau$  is the typical time scale of pattern growth in Eq. (7). **b**, Velocity autocorrelations in the solutions of Eqs. (2) decay on the order of the pattern growth scale  $\tau$  (Methods). **c**, Tracer particles advected by active turbulence move ballistically on time-scales  $t \ll \tau$  and diffusively for  $t > \tau$ . **d**, Sample trajectories of tracer particles in monochromatic random flow fields (Methods) that were periodically updated after time  $\tau_c$ . **e**, Vorticity fields  $\omega = -\nabla^2\psi$  corresponding to four stream functions  $\psi$  as used in panels (d-f). Stream functions were sampled from superstatistical distributions (Methods) with same temperature as in Movie 4, Fig. 2a and panels (a-c). **f**, Mean squared displacements for tracer particles in monochromatic superstatistics random flow fields agree with those for active turbulence system in panel (c). Panels (c) and (f) show PDFs of the tracer particle displacement at times indicated by the solid circles. Mean squared displacement  $\langle [\mathbf{X}_n(t) - \mathbf{X}_n(0)]^2 \rangle_n$  in (c, f) are based on 100,000 trajectories, respectively.

linearly forced Navier-Stokes equations (2), described by (Fig. 4a)

$$\dot{\mathbf{X}} = \mathbf{v}(t, \mathbf{X}). \quad (6)$$

Flow field solutions (Movie 4) of Eqs. (2) are correlated on short times scales  $t < \tau$  and become uncorrelated for  $t > \tau$  where  $\tau$  is the typical time scale of pattern growth (Fig. 4b) as specified in Eq. (7). As a consequence, tracer particles advected by solutions  $\mathbf{v}(t, \mathbf{x})$  of Eq. (2) move ballistically for  $t \ll \tau$  and diffusively for  $t > \tau$  (Fig. 4c).

To obtain a corresponding Langevin-type description, one has to replace the deterministic Navier-Stokes flow fields  $\mathbf{v}$  in Eq. (6) by a suitable sequence of randomly generated flow fields. To this end, we constructed stream function fields  $\psi(t, \mathbf{x})$  by sampling the Fourier coefficients  $\hat{\psi}_{\mathbf{k}} = |\hat{\psi}_{\mathbf{k}}| \exp(iS_{\mathbf{k}})$ . Guided by our above results (Fig. 3a), the phases  $S_{\mathbf{k}}$  were drawn uniformly from  $[0, 2\pi)$ , and the amplitudes  $|\hat{\psi}_{\mathbf{k}}|^2$  were sampled from an exponential (Boltzmann) distribution with mean  $2T_{\mathbf{k}}/(CA|\mathbf{k}|^2)$ , using the mode temperatures  $T_{\mathbf{k}}$  mea-

sured in the active turbulence simulations and the constants  $C$  and  $A$  from Eq. (3) (Methods). The sampling interval  $\tau_c$  was set to the half-width of the velocity autocorrelation function (Fig. 4b). The tracer trajectories (Fig. 4d) obtained by integrating Eq. (6) using the sampled fields (Fig. 4e) exhibit the same short-term ballistic motion and long-term diffusive behavior (Fig. 4f) as the reference process (Fig. 4c). These results show how transport in pattern-forming systems with scale selection can be approximated through transport in effectively monochromatic random fields.

In conclusion, we found that pattern-forming nonequilibrium systems can be described by emergent superstatistics if the balance of energy injection and dissipation concentrate mode energies near a fixed lengthscale. The above examples illustrate that these conditions are met by a diverse class of quantum and classical systems, regardless of the precise nature of the underlying scale selection mechanisms, driving protocols and mode-mixing nonlinearities. The compact statistical representation of dynamical pattern-forming phenomena via monochromatic random fields thus appears to hold promise with regards to the unified description and classification of nonequilibrium dynamics and transport.

- <sup>1</sup> Cross, M. C. & Hohenberg, P. C. Pattern formation outside of equilibrium. *Rev. Mod. Phys.* **65**, 851–1112 (1993).
- <sup>2</sup> Cardy, J., Falkovich, G. & Gawedzki, K. *Non-equilibrium Statistical Mechanics and Turbulence*. London Mathematical Society Lecture Note Series (Cambridge University Press, 2008).
- <sup>3</sup> Barenghi, C. F., Skrbek, L. & Sreenivasan, K. R. Introduction to quantum turbulence. *Proc. Natl. Acad. Sci. U. S. A.* **111**, 4647–4652 (2014).
- <sup>4</sup> Toschi, F. & Bodenschatz, E. Lagrangian properties of particles in turbulence. *Annu. Rev. Fluid Mech.* **41**, 375–404 (2009).
- <sup>5</sup> Duclos, G. *et al.* Topological structure and dynamics of three-dimensional active nematics. *Science* **367**, 1120–1124 (2020).
- <sup>6</sup> Wensink, H. H. *et al.* Meso-scale turbulence in living fluids. *Proc. Natl. Acad. Sci. U. S. A.* **109**, 14308–14313 (2012).
- <sup>7</sup> Ruelle, D. Non-Equilibrium Statistical Mechanics of Turbulence. *J. Stat. Phys.* **157**, 205–218 (2014).
- <sup>8</sup> Goldenfeld, N. & Shih, H.-Y. Turbulence as a Problem in Non-equilibrium Statistical Mechanics. *J. Stat. Phys.* **167**, 575–594 (2017).
- <sup>9</sup> Li, J., Horowitz, J. M., Gingrich, T. R. & Fakhri, N. Quantifying dissipation using fluctuating currents. *Nat. Commun.* **10**, 1666 (2019).
- <sup>10</sup> Shaebani, M. R., Wysocki, A., Winkler, R. G., Gompper, G. & Rieger, H. Computational models for active matter. *Nat. Rev. Phys.* **2**, 181–199 (2020).
- <sup>11</sup> Aranson, I. S. & Kramer, L. The world of the complex Ginzburg-Landau equation. *Rev. Mod. Phys.* **74**, 99–143 (2002).
- <sup>12</sup> Marchetti, M. C. *et al.* Hydrodynamics of soft active matter. *Rev. Mod. Phys.* **85**, 1143 (2013).
- <sup>13</sup> Dittrich, T. *et al.* *Quantum transport and dissipation* (Wiley-VCH, 1998).
- <sup>14</sup> Hänggi, P. & Marchesoni, F. Artificial Brownian motors: Controlling transport on the nanoscale. *Rev. Mod. Phys.* **81**, 387–442 (2009).
- <sup>15</sup> Taylor, J. R. & Stocker, R. Trade-offs of chemotactic foraging in turbulent water. *Science* **338**, 675–679 (2012).
- <sup>16</sup> Öttinger, H. *Beyond Equilibrium Thermodynamics* (Wiley, 2005).
- <sup>17</sup> Seifert, U. Stochastic thermodynamics, fluctuation theorems and molecular machines. *Rep. Prog. Phys.* **75**, 126001 (2012).
- <sup>18</sup> Gnesotto, F. S., Mura, F., Gladrow, J. & Broedersz, C. P. Broken detailed balance and non-equilibrium dynamics in living systems: a review. *Rep. Prog. Phys.* **81**, 066601 (2018).
- <sup>19</sup> Golestanian, R. Bose-einstein-like condensation in scalar active matter with diffusivity edge. *Phys. Rev. E* **100**, 010601 (2019).
- <sup>20</sup> Lohse, D. & Xia, K.-Q. Small-scale properties of turbulent rayleigh-bénard convection. *Annu. Rev. Fluid Mech.* **42**, 335–364 (2009).
- <sup>21</sup> Hino, M., Sawamoto, M. & Takasu, S. Experiments on transition to turbulence in an oscillatory pipe flow. *J. Fluid Mech.* **75**, 193–207 (1976).
- <sup>22</sup> Ciliberto, S. & Gollub, J. P. Chaotic mode competition in parametrically forced surface waves. *J. Fluid Mech.* **158**, 381–398 (1985).
- <sup>23</sup> Kudrolli, A. & Gollub, J. Patterns and spatiotemporal chaos in parametrically forced surface waves: a systematic survey at large aspect ratio. *Physica D* **97**, 133–154 (1996).
- <sup>24</sup> Corté, L., Chaikin, P. M., Gollub, J. P. & Pine, D. J. Random organization in periodically driven systems. *Nat. Phys.* **4**, 420–424 (2008).
- <sup>25</sup> Kelley, D. H. & Ouellette, N. T. Separating stretching from folding in fluid mixing. *Nat. Phys.* **7**, 477–480 (2011).
- <sup>26</sup> Schweitzer, F., Ebeling, W. & Tilch, B. Complex motion of Brownian particles with energy depots. *Phys. Rev. Lett.* **80**, 5044–5047 (1998).
- <sup>27</sup> Golestanian, R., Liverpool, T. B. & Ajdari, A. Propulsion of a molecular machine by asymmetric distribution of reaction products. *Phys. Rev. Lett.* **94**, 220801 (2005).
- <sup>28</sup> Romanczuk, P., Bär, M., Ebeling, W., Lindner, B. & Schimansky-Geier, L. Active Brownian Particles. *Eur. Phys. J. Spec. Top.* **202**, 1–162 (2012).
- <sup>29</sup> Harris, D. M., Quintela, J., Prost, V., Brun, P. T. & Bush, J. W. M. Visualization of hydrodynamic pilot-wave phenomena. *Journal of Visualization* **20**, 13–15 (2017).
- <sup>30</sup> Wildeman, S. Real-time quantitative schlieren imaging by fast fourier demodulation of a checkered backdrop. *Exp. Fluids* **59**, 97 (2018).
- <sup>31</sup> Swift, J. & Hohenberg, P. C. Hydrodynamic fluctuations at the convective instability. *Phys. Rev. A* **15**, 319–328 (1977).
- <sup>32</sup> Tuffillaro, N. B., Ramshankar, R. & Gollub, J. P. Order-disorder transition in capillary ripples. *Phys. Rev. Lett.* **62**, 422–425 (1989).
- <sup>33</sup> Douady, S. Experimental study of the Faraday instability. *J. Fluid Mech.* **221**, 383–409 (1990).
- <sup>34</sup> Kumar, K. & Tuckerman, L. S. Parametric instability of the interface between two fluids. *J. Fluid Mech.* **279**, 49–68 (1994).
- <sup>35</sup> Zhang, W. & Viñals, J. Secondary instabilities and spatiotemporal chaos in parametric surface waves. *Phys. Rev. Lett.* **74**, 690–693 (1995).
- <sup>36</sup> Kumar, K. Linear theory of Faraday instability in viscous liquids. *Proc. R. Soc. A* **452**, 1113–1126 (1996).
- <sup>37</sup> Kahouadji, L. *et al.* Numerical simulation of supersquare patterns in Faraday waves. *J. Fluid Mech.* **772**, R2 (2015).
- <sup>38</sup> Stoop, N., Lagrange, R., Terwagne, D., Reis, P. M. & Dunkel, J. Curvature-induced symmetry breaking determines elastic surface patterns. *Nat. Mater.* **14**, 337–342 (2015).
- <sup>39</sup> Lee, A. A., Vella, D. & Wettlaufer, J. S. Fluctuation spectra and force generation in nonequilibrium systems. *Proc. Natl. Acad. Sci. U.S.A.* **114**, 9255–9260 (2017).
- <sup>40</sup> Pomeau, Y. & Rica, S. Dynamics of a Model of a Super-solid. *Phys. Rev. Lett.* **72**, 2426–2429 (1994).
- <sup>41</sup> Yoo, C.-D. & Dorsey, A. T. Hydrodynamic theory of supersolids: Variational principle, effective lagrangian, and density-density correlation function. *Phys. Rev. B* **81**, 134518 (2010).
- <sup>42</sup> Heinonen, V., Burns, K. J. & Dunkel, J. Quantum hydrodynamics for supersolid crystals and quasicrystals. *Phys. Rev. A* **99**, 063621 (2019).
- <sup>43</sup> Sokolov, A. & Aranson, I. S. Physical properties of collective motion in suspensions of bacteria. *Phys. Rev. Lett.* **109**, 248109 (2012).
- <sup>44</sup> Bratanov, V., Jenko, F. & Frey, E. New class of turbulence

- in active fluids. *Proc. Natl. Acad. Sci. U. S. A.* **112**, 15048–15053 (2015).
- <sup>45</sup> Doostmohammadi, A., Ignés-Mullol, J., Yeomans, J. M. & Sagués, F. Active nematics. *Nat. Commun.* **9**, 3246 (2018).
- <sup>46</sup> Beck, C., Cohen, E. G. & Swinney, H. L. From time series to superstatistics. *Phys. Rev. E* **72**, 1–8 (2005).
- <sup>47</sup> O’Connor, P., Gehlen, J. & Heller, E. J. Properties of random superpositions of plane waves. *Phys. Rev. Lett.* **58**, 1296–1299 (1987).
- <sup>48</sup> Heller, E. J. Bound-state eigenfunctions of classically chaotic hamiltonian systems: Scars of periodic orbits. *Phys. Rev. Lett.* **53**, 1515–1518 (1984).
- <sup>49</sup> Plisson, T., Bourdel, T. & Müller, C. A. Momentum isotropisation in random potentials. *Eur. Phys. J. Spec. Top.* **217**, 79–84 (2013).
- <sup>50</sup> Beresnev, I. A. & Nikolaevskiy, V. N. A model for nonlinear seismic waves in a medium with instability. *Physica D* **66**, 1–6 (1993).
- <sup>51</sup> Tribelsky, M. I. Patterns in dissipative systems with weakly broken continuous symmetry. *Phys. Rev. E* **77**, 035202 (2008).
- <sup>52</sup> Slomka, J. & Dunkel, J. Spontaneous mirror-symmetry breaking induces inverse energy cascade in 3D active fluid. *Proc. Natl. Acad. Sci. U.S.A.* **114**, 2119–2124 (2017).
- <sup>53</sup> Harris, D. M. & Bush, J. W. M. Generating uniaxial vibration with an electrodynamic shaker and external air bearing. *J. Sound Vib.* **334**, 255–269 (2015).
- <sup>54</sup> Faraday, M. On a peculiar class of acoustical figures; and on certain forms assumed by groups of particles upon vibrating elastic surfaces. *Philos. Trans. Royal Soc.* **121**, 299–340 (1831).
- <sup>55</sup> Benjamin, T. B. & Ursell, F. The Stability of the Plane Free Surface of a Liquid in Vertical Periodic Motion. *P. Roy. Soc. A-Math. Phys.* **225**, 505–515 (1954).
- <sup>56</sup> Bush, J. W. M. Pilot-wave hydrodynamics. *Annu. Rev. Fluid Mech.* **47**, 269–292 (2015).
- <sup>57</sup> Tuffillaro, N. B., Ramshankar, R. & Gollub, J. P. Order-Disorder Transition in Capillary Ripples. *Phys. Rev. Lett.* **62**, 422–425 (1989).
- <sup>58</sup> Burns, K. J., Vasil, G. M., Oishi, J. S., Lecoanet, D. & Brown, B. P. Dedalus: A flexible framework for numerical simulations with spectral methods. *Phys. Rev. Res.* **2**, 838 (2020).
- <sup>59</sup> Slomka, J., Suwara, P. & Dunkel, J. The nature of triad interactions in active turbulence. *J. Fluid Mech.* **841**, 702–731 (2018).

## Acknowledgments

We thank Tapio Ala-Nissilä, Geoffrey Vasil and Martin Zwierlein for helpful discussions. This work was supported by a Complex Systems Scholar Award from the James S. McDonnell Foundation (J.D.) and the Robert E. Collins Distinguished Scholarship Fund (J.D.). P.J.S. gratefully acknowledges financial support from the NSF through CBET-2144180. V.H. has been supported by the Academy of Finland via the project No. 339228.

## Author contributions

V.H., J.S. and J.D. developed the theory. V.H. performed analytical calculations, numerical simulations of the GNS model and statistical analysis. K.J.B. contributed the quantum chaos simulations. A.J.A. and P.J.S. performed

the experiments and Faraday wave reconstruction. V.H. and J.D. wrote the paper with input from all co-authors.

## Competing financial interests

The authors declare no competing financial interests.

## Methods

**Faraday wave experiments.** A schematic of the experimental setup is presented in Fig. S1. An acrylic sheet with a star-like cut out was fitted inside a circular aluminum bath. For the results discussed in the main text, the shape of the inner boundary was given by  $R(\theta) = R_b + A_b \cos(k_b \theta)$  with  $R_b = 66.8$  mm,  $A_b = 8.1$  mm, and  $k_b = 8$  (Fig. S1b). Other boundary shapes were also tested (see Supplementary Information). The inner cavity was filled up to  $H = 1.7$  mm with deionized water with density  $\rho = 998$  kg m<sup>-3</sup>, viscosity  $\nu = 1$  cSt, and surface tension  $\sigma = 72.8$  mN m<sup>-1</sup>. A meniscus of characteristic size  $l_c \sim 2.7$  mm spontaneously formed along the border, where  $l_c = \sqrt{\sigma/(\rho g)}$  denotes the capillary length, and  $g$  the gravitational acceleration. The bath was mounted on an optical table (Newport SG-34-4 custom breadboard, 3.0’ × 4.0’ × 4.3’’) and vibrated vertically by an electromagnetic shaker (Modal Shop, 2110E) with an external power amplifier (Modal Shop, 2050E09-FS) at acceleration  $\Gamma(t) = D \cos(\omega t)$ , where  $D$  and  $f = \omega/2\pi$  are the prescribed maximum acceleration and vibrational frequency, respectively. The shaker was connected to the bath by a thin steel rod coupled with a linear air bearing (PI L.P., 4 × 4’’ cross section, 6.5’’ long hollow bar) that ensures a spatially uniform vibration to within 0.1%.<sup>53</sup> The forcing was monitored through a data acquisition system (NI, USB-6343) with two piezoelectric accelerometers (PCB, 352C65), attached to the base plate on opposite sides of the drive shaft, and a closed-loop feedback ensured a constant acceleration amplitude to within  $\pm 0.002g$ .<sup>53</sup>

At low driving  $D$ , the fluid remains quiescent. However, as the acceleration is increased beyond a critical driving  $D_F$ , the so-called Faraday threshold, the layer becomes unstable to a standing field of monochromatic waves<sup>54</sup>. The first waves to appear are subharmonic  $\omega_F = \omega/2$ , with a wavelength  $\lambda_F = 2\pi/k_F$  prescribed by the water-wave dispersion relation  $\omega_F^2 = (gk_F + \sigma k_F^3/\rho) \tanh k_F H$ <sup>33,55,56</sup>. As the acceleration  $D$  is increased beyond  $D_F$ , nonlinearities excite additional wave modes leading to an order-disorder transition<sup>1,57</sup> beyond which the waves are subject to the chaotic motion discussed in the main text. The experiments were performed at  $D = 2.500g$  and  $f = 140$  Hz. At this frequency, the characteristic wavelength was  $\lambda_F = 4.60$  mm and the Faraday threshold  $D_F = 1.830g$ .

**Faraday wave field reconstruction.** The wave field was measured with a free-surface Schlieren technique<sup>29,30</sup> that uses a 2D periodic checkerboard pattern as a backdrop to the refractive object of interest (Fig. S3b). The periodic pattern, which was optically distorted by the presence of the waves, was recorded with a CCD camera (Allied Vision Mako U-130B, 1280 × 1024 pixels) mounted

directly above the bath. To ensure uniform normal lighting, a semi-reflective mirror at  $45^\circ$  was placed between the CCD camera and the bath, and the bath was illuminated with a diffuse-light LED panel facing the mirror horizontally. The experiments were recorded in one-minute long videos at 10 frames per second. The relative phase between the frame acquisition and driving signals was adjusted to capture the waves at an instant near maximum average amplitude. The liquid depth  $H$  was sufficiently low to prevent phase wrapping<sup>30</sup>. For the spectral analysis presented in the main text we only considered the wave-deformed pattern in a square region of  $93 \times 93$  mm centered in the bath (Fig. S3b). An FFT demodulation method<sup>30</sup> was then used to reconstruct the 3D surface Faraday waves in that region (Fig. S3c). The coefficient  $C$  in Eq. (4) is given by the surface energy density  $\sigma$  and the global temperature  $T_g = 7200 \sigma \text{cm}^2$ .

**Quantum chaos simulations.** We simulated Eqs. (1a) and (1b) in a doubly-periodic box of size  $L = 2\pi\ell$  using the pseudo-spectral code Dedalus<sup>58</sup> with  $256^2$  Fourier modes. The initial condition is a uniform plane wave,  $\psi(0, \mathbf{x}) \propto \exp(i\mathbf{k}_c \cdot \mathbf{x})$ , with wavevector  $\mathbf{k}_c = [64\ell^{-1}, 0]$  and energy  $E_c = \hbar^2 k_c^2 / 2m$ . The steady potential  $V(\mathbf{x})$  consists of a real Gaussian random field with a Gaussian correlation length of  $l_p = L/4$ . The potential is rescaled to have zero mean and a standard deviation of  $\alpha\omega_c$ , where  $\alpha$  is adjusted to control the energy concentration in Fourier space. The simulations are integrated with a second-order implicit-explicit Runge-Kutta scheme using a timestep of  $(1/80)\omega_c^{-1}$  until a time of  $T = 4 \times 10^5 \omega_c^{-1}$ . For improved numerical conditioning, the system is non-dimensionalized by taking  $\hbar = m = \ell = 1$ . For data in Fig. 3 we let the system relax for time  $10^5 \omega_c^{-1}$  before analyzing the data. The coefficient  $C$  in Eq. (4) is given by  $\hbar^2/m$  and the global temperature  $T_g = 0.680 \hbar^2/L^2/m$ .

**Active turbulence simulations.** We simulated Eqs. (2) using the pseudo-spectral code described in Ref.<sup>59</sup> using  $365^2$  modes. The typical pattern growth timescale is

$$\tau = \left[ \frac{\Gamma_2}{2\Gamma_4} \left( \Gamma_0 - \frac{\Gamma_2^2}{4\Gamma_4} \right) \right], \quad (7)$$

and the width of the energy shell (Fig. 2c) reflects the bandwidth

$$\kappa = \left( \frac{-\Gamma_2}{\Gamma_4} - 2\sqrt{\frac{\Gamma_0}{\Gamma_4}} \right)^{1/2}$$

of active Fourier modes. For all the simulations we set the characteristic vortex size  $\Lambda = 1$  (see main text),  $\tau = 1$ , and  $\kappa = 0.3/\Lambda$ . The simulations are performed in a periodic box with size  $(100\Lambda \times 100\Lambda)$  corresponding to roughly  $100^2$  vortices. The time step used for all the simulations was  $0.01\tau$ . The simulations are initialized with a random stream function  $\psi$  taking uniformly distributed random values between zero and  $10^{-6}$ . After this the simulation is run for  $10\tau$  ( $10^3$  time steps) to ensure full

development of pattern turbulence before any statistical analysis. For the data in 3 we ran the simulation for  $50,000\tau$  ( $5 \times 10^6$  time steps) creating 10,000 outputs at uniform time intervals. The panels in Fig. 2 corresponding to active turbulence simulations are taken from a representative time step after the initial relaxation. The coefficient  $C$  in Eq. (4) is given by the mass density of the suspension and the global temperature  $T_g = 530 \rho\Lambda^4/\tau^2$ .

**Fitting the inverse tail temperature  $\beta_t$ .** Here we describe the fitting procedure for the inverse tail temperature in Eq.(5). Since  $C_f$  is determined by the requirement that  $f$  integrates to unity, only  $\beta_t$  remains as a free parameter. Here we describe the fitting procedure used to obtain the inverse tail temperature  $\beta_t$ . We introduce a splitting of the probability density  $f$  in terms of the ring and the tail contributions. Let,

$$f(\mathcal{E}) = f_t(\mathcal{E}; \beta_t) + f_r(\mathcal{E}; \beta_t),$$

where  $f_t$  and  $f_r$  correspond to the first and the last term, respectively, in Eq. (5). The inverse energy scale  $\beta_t$  is expected to be much larger than 1. This implies that  $f_t$  only contributes to the small energy scales of the probability distribution function. Let  $f_e$  be the empirical probability distribution function obtained from simulations or experiments. We start by making a guess  $\beta_t = \beta_t^{(0)}$  to calculate  $f_r$ . The normalization constant  $C_f$  can be obtained by matching the integrated probabilities  $\int_{\mathcal{E}_0}^{\infty} d\mathcal{E} f$  for  $f_e$  and  $f_r$  with some large  $\mathcal{E}_0$ . This lets us calculate

$$\log[(f_e - f_r) \mathcal{E}] \approx -\beta_t^{(1)} \mathcal{E} - \frac{1}{2} \log(\log \beta_t^{(1)}) + \log C_f$$

Now the parameter  $\beta_t^{(1)}$  can be obtained from a linear fit for small values of  $\mathcal{E}$  and we can start the process again by calculating  $f_r$  using  $\beta_t^{(1)}$ . We continue this process until  $\beta_t$  converges.

**Colorbars in Figure 2.** The color bar limits in Fig. 2a and c are the maxima and the minima of the observed fields. In panel b, the color bars range from lowest 2.5 percentile up to the 97.5 percentile of the energy density data, respectively, to increase visibility of the characteristic scars.

**Tracer particle dynamics.** The active turbulence system was ran for  $50\tau$  after initial relaxation creating 4000 time frames. Other simulation details are as described before. We define the velocity autocorrelation as  $\langle \mathbf{v}(0) \cdot \mathbf{v}(t) \rangle / \langle |\mathbf{v}(0)|^2 \rangle$ , where the averages are taken over velocities at every second grid point. The corresponding monochromatic random field is created by sampling the squared amplitudes of the Fourier coefficients of the stream function  $|\hat{\psi}_{\mathbf{k}}|^2$  from a superstatistics distribution Eq. (5), while the phases are sampled uniformly. We limit the Fourier coefficients to a ring in  $\mathbf{k}$  space with a radius  $k_c$ . The width of the ring is set by the bandwidth scale  $\kappa = 0.3/\Lambda$ . We fix the average amplitudes of the Fourier coefficients by matching the average kinetic energies of the random system and the simulated active turbulence system. This corresponds to matching the temperatures.



For both of the systems, we set up random initial conditions for 100,000 tracer particles to gather the statistics of the mean squared displacement. To update the positions of the particles in time we use a central difference method where the position  $\mathbf{X}_{t_n}$  at discrete time  $t_n$  is

calculated as  $\mathbf{X}_{t_n} = \mathbf{X}_{t_{n-1}} + \Delta t(\mathbf{v}(t_{n-1}, \mathbf{x}) + \mathbf{v}(t_n, \mathbf{x}))/2$ . Here  $\Delta t = 0.01\tau$  is the time step between the time frames and the position  $\mathbf{x}$  corresponds to the finite grid point closest to  $\mathbf{X}_{t_n}$ .